Nanoscale

COMMUNICATION

View Article Online
View Journal | View Issue

Cite this: *Nanoscale*, 2019, **11**, 50

Received 22nd October 2018,
Accepted 25th November 2018

DOI: 10.1039/c8nr08457b

rsc.li/nanoscale

Urchin-like NiO–$NiCo_2O_4$ heterostructure microsphere catalysts for enhanced rechargeable non-aqueous Li–O_2 batteries†

Wen Zhao,[a] Xiaomin Li,[a] Rui Yin,[a] Lei Qian,*[a] Xiaoshuai Huang,[a] Hu Liu,[b,c] Jiaoxia Zhang,[b,d] Jun Wang,[a] Tao Ding*[e] and Zhanhu Guo*[b]

Urchin-like NiO–$NiCo_2O_4$ microspheres with heterostructures were successfully synthesized through a facile hydrothermal method, followed by thermal treatment. The unique structure of NiO–$NiCo_2O_4$ with the synergetic effect between $NiCo_2O_4$ and NiO, and the heterostructure favour the catalytic activity towards Li–O_2 batteries. $NiCo_2O_4$ is helpful for boosting both the oxygen reduction reaction and oxygen evolution reaction for the Li–O_2 batteries and NiO is likely to promote the decomposition of certain by-products. The special urchin-like morphology facilitates the continuous oxygen flow and accommodates Li_2O_2. Moreover, benefitting from the heterostructure, NiO–$NiCo_2O_4$ microspheres are able to promote the transport of Li ions and electrons to further improve battery performance. Li–O_2 batteries utilizing a NiO–$NiCo_2O_4$ microsphere electrode show a much higher specific capacity and a lower overpotential than those with a Super P electrode. Moreover, they exhibit an enhanced cycling stability. The electrode can be continuously discharged and charged without obvious terminal voltage variation for 80 cycles, as the discharge capacity is restricted at 600 mA h g^{-1}, suggesting that NiO–$NiCo_2O_4$ is a promising catalyst for Li–O_2 batteries.

1. Introduction

The increasing demand for future energy storage systems has driven rapid growth of battery research.[1,2] In order to meet the target for applications in electric vehicles and grid storage, various battery systems, such as lithium–ion, lithium–sulphur and metal–air batteries, have been studied.[3–7] Recently, Li–O_2 batteries have attracted enormous attention due to their extremely high theoretical energy density and potential applications in transportation, portable electronics and grid energy storage.[8–10] The discharge and charge processes in Li–O_2 batteries are related to the oxygen reduction reaction (ORR) and the oxygen evolution reaction (OER), respectively.[11–13] The practical applications of Li–O_2 batteries have been restricted by many problems, including high discharge/charge overpotential caused by sluggish reaction kinetics,[14–16] electrolyte decomposition under high voltage, and safe issues resulting from the active Li anode.[17–19] Developing bifunctional electrocatalysts to efficiently catalyse both the ORR and OER is one of the keys to achieve high performance Li–O_2 batteries. The electrocatalysts should be able to facilitate the rapid decomposition of discharge products to improve the capacity, round-trip efficiency and cycling stability performance of Li–O_2 batteries.[20–22]

Although noble metals and their alloys have been proved to be efficient bifunctional catalysts,[23–25] high electrocatalytic performance transition metal oxides, such as Co_3O_4,[26–29] MnO_2,[30–32] $MnCo_2O_4$,[33–35] and $NiCo_2O_4$,[36–38] are more suitable for practical uses because of their low cost and abundant reserves. Among them, $NiCo_2O_4$ is one of the most promising materials due to its large amount of catalytic active sites from two redox couples of Co^{3+}/Co^{2+} and Ni^{3+}/Ni^{2+}.[20,39] Besides, compared with NiO and Co_3O_4, $NiCo_2O_4$ possesses enhanced electrical conductivity.[40,41] It has also been reported that the microstructure of catalysts significantly influenced their catalytic activity.[39,42–44] In order to obtain a better Li–O_2 battery performance, $NiCo_2O_4$ cathode catalysts with various microstructures have been prepared and studied, such as nanotubes, nanoflakes, nanosheets, nanowire arrays and microspheres.[40,45–48]

[a]*Key Laboratory for Liquid-Solid Structural Evolution and Processing of Materials (Ministry of Education), Shandong University, 17923 Jingshi Road, Jinan 250061, China. E-mail: qleric@sdu.edu.cn, jw707@sdu.edu.cn*
[b]*Integrated Composites Lab (ICL), Department of Chemical & Biomolecular Engineering, University of Tennessee, Knoxville, TN 37996, USA. E-mail: zguo10@utk.edu*
[c]*Key Laboratory of Materials Processing and Mold (Zhengzhou University), Ministry of Education, National Engineering Research Center for Advanced Polymer Processing Technology, Zhengzhou University, Zhengzhou, 450002, China*
[d]*School of Material Science and Engineering, Jiangsu University of Science and Technology, Zhenjiang, Jiangsu, 212003, China*
[e]*College of Chemistry and Chemical Engineering, Henan University, Kaifeng 475004, P. R. China. E-mail: dingtao@henu.edu.cn*

†Electronic supplementary information (ESI) available. See DOI: 10.1039/c8nr08457b

Recently, urchin-like $NiCo_2O_4$ microspheres have attracted great interest, owing to their high specific surface area, short diffusion path for ions or electrons and enough channels for mass transport, which are in favour of higher electrocatalytic performance for Li–O_2 batteries.[39,49] However, Li–O_2 batteries based on single phase metal oxides still suffer from poor capacities, high overpotential and unsatisfactory cycling stability which limited their practical applications. Therefore, many efforts have been made to design novel hybrid electrodes in order to achieve synergetic effects between two components. For instance, it has been reported that one-dimensional RuO_2/Mn_2O_3 fibers,[50] RuO_2-δ-MnO_2 nanosheets,[32] mesoporous $ZnO/ZnFe_2O_4$ nanocages,[51] Fe_2O_3@MnO_2 composites,[52] and NiO–RuO_2 nanoparticles[53] were prepared and they exhibited favourable battery performance because of the synergetic effects between two components.

Compared with mixture or homogeneous doping bulk, heterostructures constructed from coupling nanocrystals with different band gaps have great potential applications in photocatalysis, sensors and energy storage because of their interface effects which offer unprecedented properties.[54] Benefiting from the existing internal electric field, heterostructures are able to enhance the surface reaction kinetics as well as to facilitate charge transport.[55,56] Thus, from the perspective of enhancing the electronic conductivity and ion diffusion capability, the design and fabrication of a complex heterostructure by employing two different materials might be a feasible strategy to obtain better electrocatalytic performance in Li–O_2 batteries. It was also found that NiO played an important role in decomposing the by-products containing carbonate/carboxylate species.[57,58] The NiO catalyst can promote the formation of thinner passivation layers to avoid the hindrance of charge transfer from the cumulative passivation layers.[58] Therefore, the NiO catalyst can facilitate efficient oxidation of carbonate/carboxylate species, as well as promote the peroxide oxidation. Mixed metal oxides containing NiO were designed to improve their electrocatalytic performance.[59] For example, Tan *et al.*[60] reported a nanostructured RuO_2/NiO cathode which enabled the lithium–air batteries to be truly operated in ambient air at 500 mA h g^{-1} for 200 cycles. Liu *et al.*[61] developed a method for synthesizing ultrafine NiO/CoO catalysts which retained a capacity of >1000 mA h g^{-1} after 100 cycles. Many previous studies have successfully employed the NiO–$NiCo_2O_4$ composite as the electrode for supercapacitors, and the composites exhibited good catalytic activity towards the ORR and OER.[62–66] Nevertheless, there are far few reports on NiO–$NiCo_2O_4$ composites used as cathode catalysts for Li–O_2 batteries. They are expected to effectively facilitate the formation and decomposition of Li_2O_2 with less by-product accumulation during cycling.

Herein, inspired by the unique advantages of heterostructures and the benefits of NiO–$NiCo_2O_4$ composites, we proposed and constructed NiO–$NiCo_2O_4$ microspheres with a heterostructure through a facile hydrothermal method following annealing treatment. This unique structure was able to promote fast transport of ions and electrons to obtain enhanced battery performance. The capacity, reversibility and rate performance of the batteries were investigated by electrocatalytic testing and the results demonstrated that the NiO–$NiCo_2O_4$ microspheres with the heterostructure were favourable for the catalytic activity of nonaqueous Li–O_2 batteries.

2. Experimental

2.1 Preparation of NiO–$NiCo_2O_4$ microspheres with the heterostructure

In a typical hydrothermal preparation process, 1.25 mmol $NiCl_2{\cdot}6H_2O$, 2.5 mmol $CoCl_3{\cdot}6H_2O$ and 4.5 mmol urea were dissolved in 25 mL deionized water at room temperature and the solution was ultrasonically treated for 30 minutes. It was then transferred to a 50 mL stainless steel autoclave with a Teflon liner and was heated to 120 °C and maintained for 8 hours. After being cooled down to room temperature, the product was collected by centrifugation and washed with deionized water and ethanol several times, followed by drying at 60 °C under vacuum for 12 h. Finally, the obtained product was calcined at different temperatures for 3 h with a heating rate of 2 °C min^{-1} in air to obtain urchin-like heterostructure NiO–$NiCo_2O_4$ microspheres. Different NiO–$NiCo_2O_4$ microspheres were fabricated by applying calcination temperatures of 400, 500 and 600 °C and they were designated as NCO-400, NCO-500 and NCO-600, respectively.

2.2 Materials characterization

X-ray diffraction (XRD) patterns were recorded on a D8 Advance X-ray diffractometer using Cu Kα radiation (λ = 1.5418 Å). X-ray photoelectron spectroscopy (XPS) was carried out on a ThermoFisher K-Alpha instrument. The XPS data were analysed by CasaXPS software and all the results were calibrated by using C 1s = 284.6 eV. The morphology and microstructure of the synthesized materials were examined using a field emission scanning electron microscope (FESEM: SU-70) equipped with an energy dispersive X-ray (EDX) analyser and a transmission electron microscope (TEM: JEOL-JEM2100, operated at 200 kV).

2.3 Electrochemical investigation

The electrochemical performance of the Li–O_2 batteries was analysed using a 2032-type coin cell with holes in its top cover. To prepare the electrodes tested in Li–O_2 cells, 40 wt% catalyst, 40 wt% Super P carbon and 20 wt% poly(tetrafluoroethylene) were mixed in isopropanol to prepare a slurry, which was homogeneously dispersed on a carbon paper (TGP-H-060, Toray) and dried at 120 °C under vacuum for 12 h. All the cells were assembled in a glovebox under an Ar atmosphere, in which both oxygen and water contents were less than 0.1 ppm. Li–O_2 batteries consist of a Li foil anode, a glass fibre separator soaked with the electrolyte containing 1 M lithium bis(trifluoromethanesulfonyl)imide in triethylene glycol dimethyl ether (LiTFSI/TEGDME) and a catalyst coated oxygen cathode. Galvanostatic discharge/charge tests were carried out in an O_2-purged chamber on a multichannel battery testing system (LAND CT 2001A) in the potential range of 2.35–4.35 V at

current densities of 100, 200, 300, 400 and 500 mA g^{-1}, respectively. The specific capacities were calculated based on the amount of the active material in the cathodes. Cyclic voltammetry (CV) was performed on an electrochemical workstation (RST5002F) at a scan rate of 0.1 mV s^{-1} in the potential range of 2.35–4.35 V (*vs.* Li/Li^+). Electrochemical impedance spectroscopy (EIS) was tested on the same electrochemical workstation using a sine wave of 0.01 V amplitude over a frequency range of 100 kHz–0.01 Hz.

3. Results and discussion

The synthetic procedure of NiO–$NiCo_2O_4$ microspheres with a heterostructure, shown in Fig. 1, was carried out through a two-step route. Firstly, the NiO–$NiCo_2O_4$ precursor was prepared by a hydrothermal reaction. Afterwards, the precursor was calcined to achieve NiO–$NiCo_2O_4$ heterostructure microspheres. The crystal structure and composition of the as-prepared materials were characterized by XRD analysis. The XRD pattern (Fig. S1a†) of the precursor revealed that it was composed of cobalt–nickel bimetallic carbonate hydroxide. Fig. 2a shows the XRD pattern of the as-prepared NiO–$NiCo_2O_4$ microspheres with different calcination temperatures. All the peaks matched well with the cubic $NiCo_2O_4$ (JCPDS no.: 20-0781) and cubic NiO (JCPDS no.: 65-5745), which clearly demonstrated that the synthesized products were composed of $NiCo_2O_4$ and NiO. No presence of the NiO peak was observed in the XRD result of NCO-400, while the cubic phase of NiO peaks appeared in the XRD result of NCO-500 and NCO-600. This

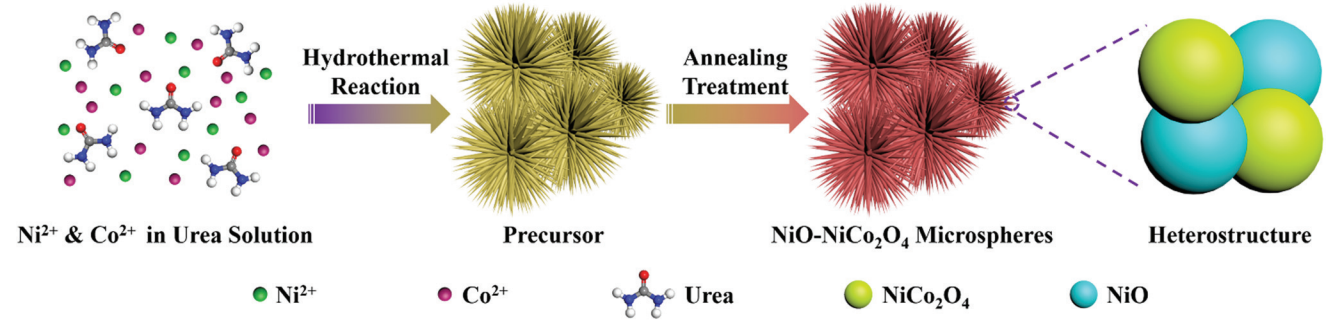

Fig. 1 Schematic illustration of the formation of NiO–$NiCo_2O_4$ microspheres through a two-step method.

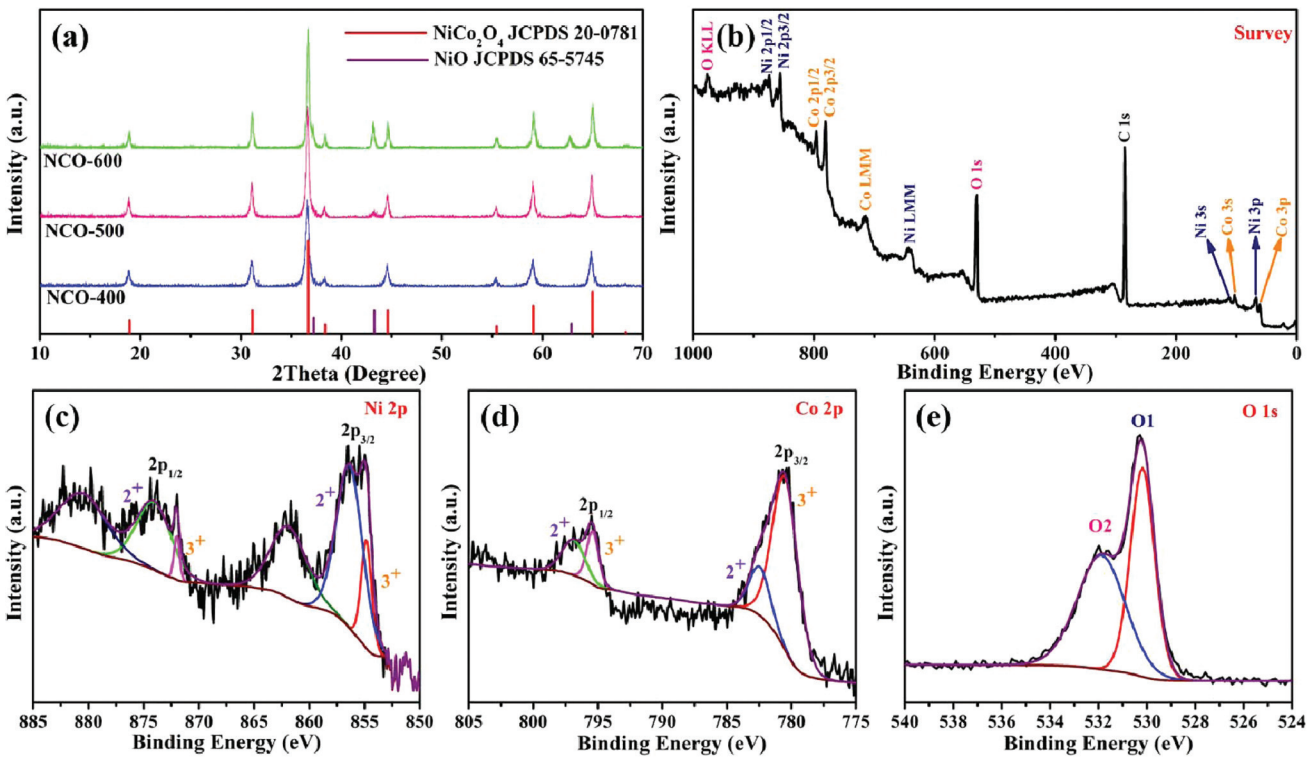

Fig. 2 (a) XRD patterns of NCO-400, NCO-500 and NCO-600; XPS spectra of NCO-500: (b) survey, (c) Ni 2p, (d) Co 2p and (e) O 1s.

was consistent with the observation of the NiO phase when the firing temperature was raised to 500 °C.[67] The cubic NiO phase was initially formed in the sample annealed at 500 °C and co-existed with $NiCo_2O_4$ as surface coverage. It was possibly because the spinel $NiCo_2O_4$ was decomposed with the loss of NiO.[67–69] However, the specific mechanism still needs further study to confirm.

XPS measurement was carried out to further understand the chemical composition and the elemental oxidation state of NiO–$NiCo_2O_4$ samples. Fig. 2b shows the survey spectrum of NCO-500, which indicates the presence of C, O, Co and Ni elements. In Fig. 2c of the high-resolution spectrum of Ni 2p, the peaks were well-fitted with two spin–orbit doublets and two shakeup satellite peaks. The fitting peaks with binding energies of 856.5 and 874.1 eV were indexed to Ni^{2+} signals, while the peaks with those of 854.8 and 872.0 eV were indexed to Ni^{3+} signals. The satellite peaks at 861.9 and 880.7 eV were shakeup peaks of Ni.[70,71] In a similar way, Co 2p can be fitted to two spin–orbit doublets (Fig. 2d). The fitting peaks at 782.5 and 797.0 eV were indexed to Co^{2+} signals, while the peaks at 780.4 and 795.4 eV were indexed to Co^{3+} signals.[71,72] These results indicated that in NCO-500, both Ni and Co were partially oxidized and reduced, respectively, to balance the formation of oxygen vacancies.[73,74] The spectrum of O 1s (Fig. 2e) shows two oxygen contributions. The fitting peak at 530.1 eV is assigned to the metal–oxygen bond, and the peak at 531.8 eV is usually associated with a high number of defect sites.[75,76]

The morphology and microstructure of the NiO–$NiCo_2O_4$ samples were characterized by FESEM and TEM. The images in Fig. S1b† show the morphology of the NiO–$NiCo_2O_4$ precursor. It generally presented a spherical urchin shape structure with a uniform diameter of about 5 μm. The FESEM images of the as-prepared NCO-500 in Fig. 3a and c show that the structure did not change after calcination. It was observed from Fig. 3a that each urchin-like NCO-500 sphere displayed a uniform diameter of 5 μm with numerous small nanorods radially-grown from the center. The elements in the NCO-500 sample were characterized by EDS and the results are shown in Fig. 3b, which confirmed the presence of Ni, Co and O elements. Element mapping results in Fig. 3d, e and f show the uniform distribution of Ni, Co and O elements in an NCO-500 sphere. The FESEM images of NCO-400 and NCO-600 with the according element mapping results are shown in Fig. S2 and S3,† respectively, and the morphology is similar to that of NCO-500.

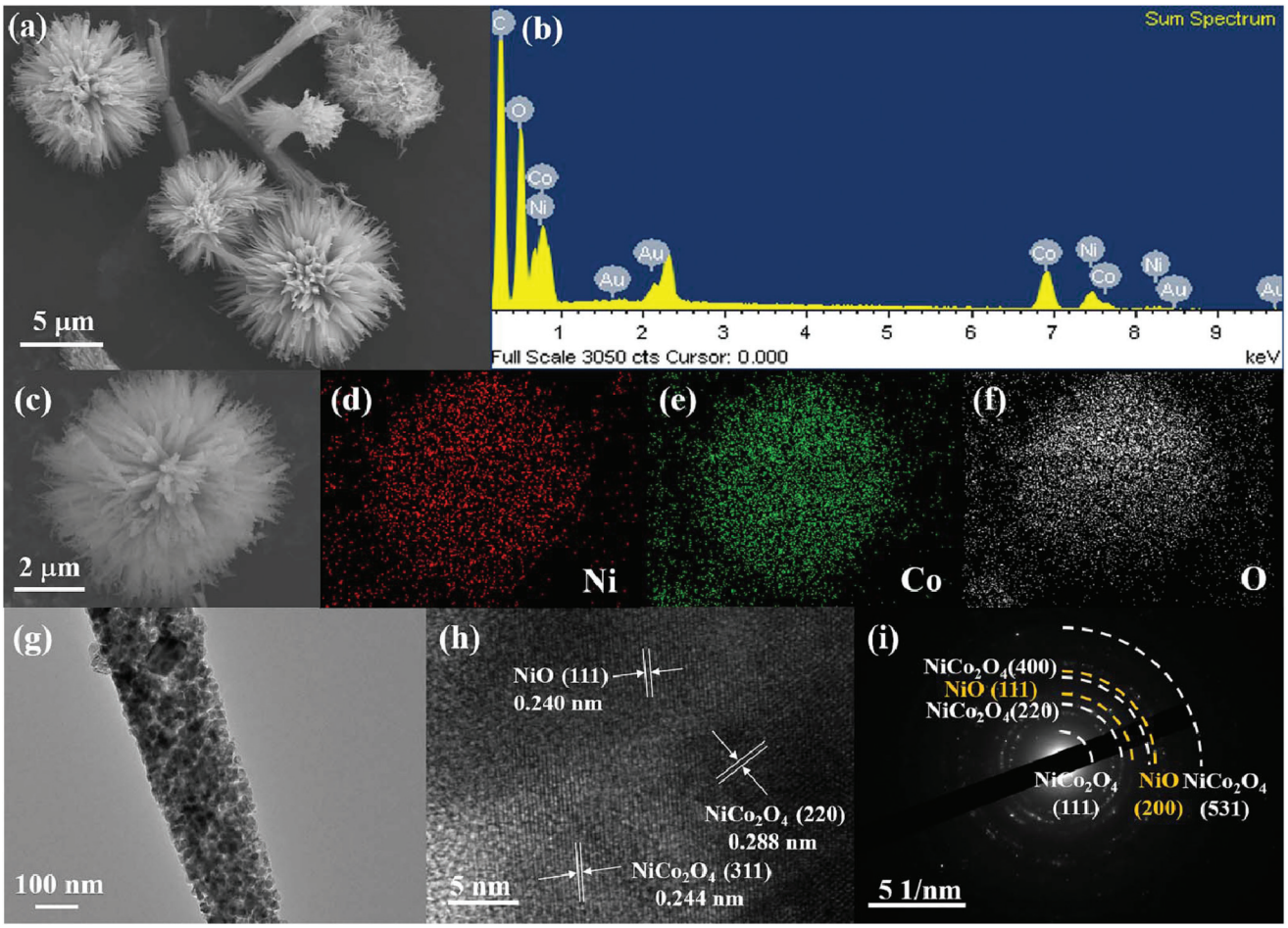

Fig. 3 FESEM images of NCO-500 at (a) low and (c) high magnifications; (b) EDS result of NCO-500; element mapping images of NCO-500: (d) Ni, (e) Co and (f) O; (g) TEM images of NCO-500; (h) high resolution TEM image; (i) selected area electron diffraction of NCO-500.

NCO-500 was tested for TEM to further examine its detailed morphology and component structure. Fig. 3g shows the nanorods which constituted the NiO–$NiCo_2O_4$ urchin-like microspheres. The HRTEM image in Fig. 3h clearly presents the lattice fringes with spacings of about 0.288, 0.244 and 0.240 nm, corresponding to the (220) and (311) planes of $NiCo_2O_4$ and the (111) planes of NiO, respectively, which are consistent with the results of the XRD pattern. The corresponding SAED pattern in Fig. 3h shows well-defined rings indexed to the NiO and spinel $NiCo_2O_4$ phases, indicating the polycrystalline characteristic of NiO–$NiCo_2O_4$ urchin-like microspheres.

Different CV curves of the Li–O_2 cells containing the NiO–$NiCo_2O_4$ microspheres and pure SP electrodes in the LiTFSI/TEGDME electrolyte were studied, as shown in Fig. S4.† Compared with the pure SP electrode, the NiO–$NiCo_2O_4$ electrodes exhibited considerably larger cathodic and anodic current values and higher cathodic potentials, indicating higher bifunctional electrocatalytic activity towards the ORR and OER in non-aqueous Li–O_2 batteries. Particularly, the NCO-500 electrode showed the highest current value among all samples, indicating its excellent catalytic activity. As a result, it demonstrated that the NiO–$NiCo_2O_4$ electrode may have remarkable electrochemical properties towards both the formation and decomposition of discharge products during discharge and charge processes.

The Li–O_2 battery performances of NiO–$NiCo_2O_4$ heterostructure microspheres and pure SP electrodes were further studied by galvanostatically discharge and charge tests. Fig. 4a shows the initial full discharge/charge profiles for the Li–O_2 batteries with NCO-400, NCO-500, NCO-600 and pure SP electrodes at a current density of 100 mA g^{-1} from 2.35 to 4.35 V *vs.* Li^+/Li. The NiO–$NiCo_2O_4$ based Li–O_2 battery showed a lower overpotential and a much higher specific capacity than that of a pure SP based Li–O_2 battery. The discharge/charge capacities of the pure SP electrode were 1750/1619 mA h g^{-1}. The electrodes with NiO–$NiCo_2O_4$ exhibited dramatically improved discharge/charge capacities. In brief, the NCO-400, NCO-500 and NCO-600 electrodes delivered discharge/charge capacities of 7092/7563, 9231/8349 and 5429/4622 mA h g^{-1}, respectively. In order to eliminate the capacity influence of the carbon paper, a Li–O_2 cell using only the carbon paper as a cathode material was also assembled. It was observed from Fig. S5† that the discharge/charge capacities of the carbon paper were quite limited, indicating that the contribution of the carbon paper to the total capacity was negligible. Therefore, it is reasonable to use carbon paper as the current collector in the testing of Li–O_2 batteries.

In Fig. 4b, as the current densities varied from 200, 300, 400 to 500 mA g^{-1}, the NCO-500 electrode also showed a relatively high discharge/charge performance of 8406/8162, 5461/4257, 4113/3292 and 3711/2254 mA h g^{-1}, respectively, indicating that the NCO-500 composite delivered a good rate capability. Fig. 4c exhibits the typical initial discharge and charge profiles of the NCO-500 electrode and the SP electrode with a fixed capacity of 600 mA h g^{-1} at a current density of 100 mA g^{-1}. The NCO-500 electrode showed a much lower discharge and charge overpotential. Fig. 4d exhibits the selected discharge/charge profiles for the NCO-500 electrode at a current density of 100 mA g^{-1} with a fixed specific capacity of 600 mA h g^{-1} and the specific capacity showed no loss up to 80 cycles. The cycling stability of the NCO-500 and SP based electrodes was also manifested by the discharge/charge terminal voltage at the current density of 100 mA g^{-1} with a fixed capacity of 600 mA h g^{-1}, and the NCO-500 electrode demonstrated a favourable cycling performance for the Li–O_2 batteries. As shown in Fig. 4e, the discharge/charge terminal voltage for the NCO-500 electrode remained stable over 80 cycles (2.32 and 4.25 V respectively), while for the SP electrode, its discharge terminal voltage dropped quickly after the first 2 cycles.

Table S1† summarizes the Li–O_2 battery performance of the NCO-500 electrode in comparison with some representative NiO-based and $NiCo_2O_4$-based electrodes reported in the literature. It clearly demonstrated that the NCO-500 composite electrode showed a better performance than most of the other electrodes under similar testing conditions, especially in terms of capacity and cycling stability, making the NCO-500 composite a promising material for advanced Li–O_2 batteries. Compared with other NiO-based and $NiCo_2O_4$-based materials, NCO-500 combined the benefits of NiO and $NiCo_2O_4$. The synergetic effect between $NiCo_2O_4$ and NiO favors enhancing the catalytic activity towards Li–O_2 batteries. $NiCo_2O_4$ can help boost both the ORR and OER, while NiO is likely to promote the decomposition of certain by-products. Moreover, the unique urchin-like heterostructure also provides advantages. The special morphology facilitates the continuous oxygen flow and the heterostructure promotes the transport of Li ions and electrons to further improve the battery performance.

EIS analysis was also conducted on different samples in the frequency range from 0.01 Hz to 10 kHz, as shown in Fig. 5a. Each curve consists of two parts, a small semicircle at the high-frequency region attributes to the charge-transfer resistance and a slope line at the low-frequency region is associated with the ion diffusion process within the electrode.[76–78] From the Nyquist plots, it was found that the NCO-500 electrode delivered the lowest charge transfer resistance among all the four samples, indicating that it enabled an efficient charge transport on the electrode/electrolyte interface and ensured the electrochemical activity during cycling. The EIS test of the NCO-500 electrode at different discharge/recharge stages (Fig. 5b) was also performed to further identify the discharge and recharge characteristics. After the first discharge, a larger charge-transfer resistance was observed compared with that of the fresh electrode. This is because of the formation and accumulation of Li_2O_2 on the electrode, which was hypothesized to prevent the transfer of electrons and lead to high electrical resistivity.[79,80] After being recharged, the charge-transfer resistance of the NCO-500 electrode slightly changed compared with that of the fresh electrode, suggesting that the formation and decomposition of the reaction product is reversible. The charge-transfer resistance experienced almost no

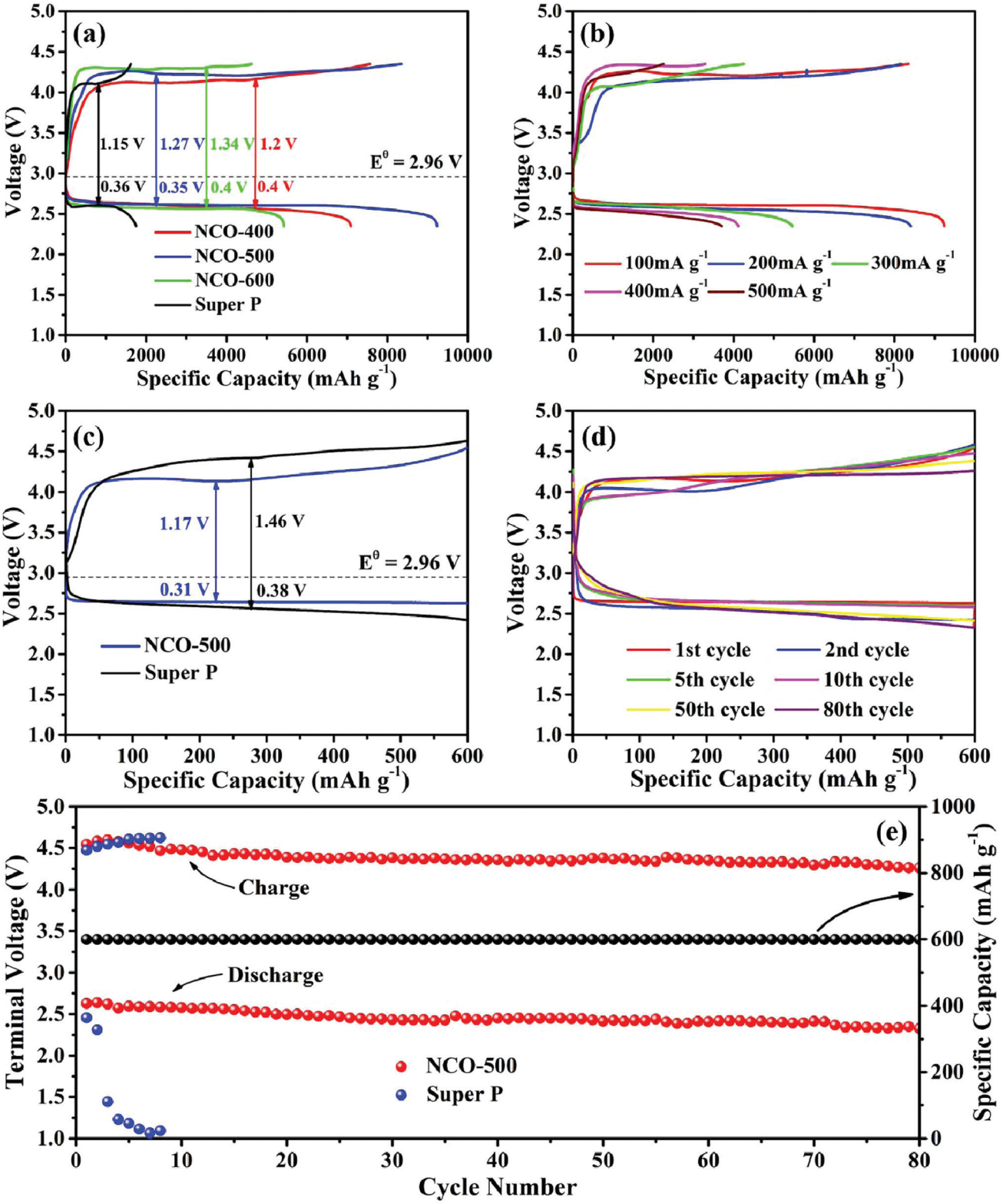

Fig. 4 The initial discharge/charge profiles of (a) NCO-400, NCO-500, NCO-600 and pure SP electrodes at 100 mA g^{-1}, (b) the NCO-500 electrode at different current densities; (c) initial discharge/charge plots of the NCO-500 and SP electrodes under a capacity limit of 600 mA h g^{-1} at 100 mA g^{-1}; (d) typical discharge/charge profiles of NCO-500 electrode under a capacity limit of 600 mA h g^{-1} at 100 mA g^{-1}; (e) cycling performances of the NCO-500 and SP electrodes under a capacity limit of 600 mA h g^{-1} at 100 mA g^{-1}.

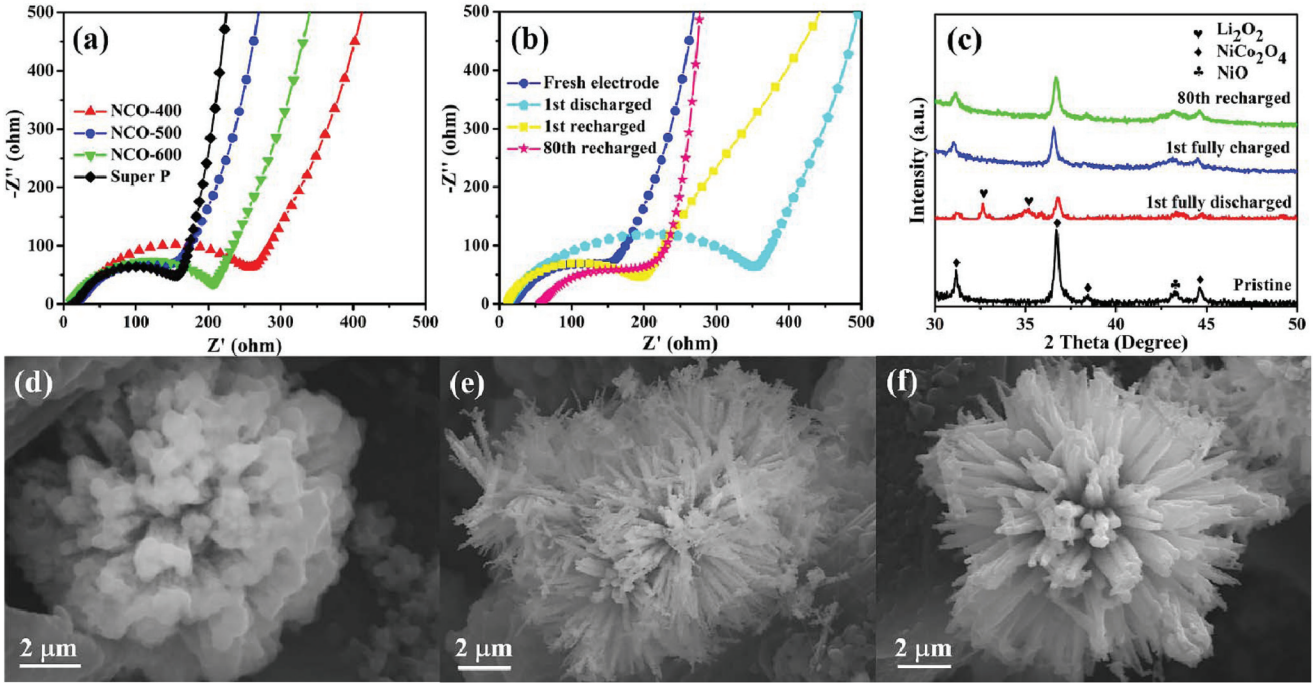

Fig. 5 (a) EIS plots of NCO-400, NCO-500, NCO-600 and SP electrodes; (b) EIS plots of NCO-500 electrodes at fresh, 1st cycle discharged, 1st cycle recharged, and 80th cycle recharged states; (c) XRD patterns of the NCO-500 electrode at fresh, 1st cycle discharged, 1st cycle recharged, and 80th cycle recharged states; FESEM images of NCO-500 electrodes at (d) the 1st cycle discharged to 2.35 V, (e) the 1st cycle recharged to 4.35 V and (f) the 80th cycle recharged stages.

change after the 80th cycle, mainly because less irreversible by-products existed on the electrode, confirming its remarkable catalytic properties.[81,82]

To have a further understanding of the changes in the composition and morphology of the NCO-500 electrode at different discharge/recharge stages, *ex situ* XRD and FESEM investigations were conducted. Fig. 5c shows the XRD patterns of the NCO-500 electrode obtained before discharge, after discharge to 2.35 V, after recharge to 4.35 V and after 80th cycle, respectively. Compared with the XRD pattern of the fresh electrode, the characteristic Li_2O_2 peaks were distinctly observed in the electrode after the 1st full discharge to 2.35 V. These two peaks were assigned to the (100) and (101) of Li_2O_2, and this indicated that Li_2O_2 is the major crystalline discharge product.[16,21,83] After being recharged to 4.35 V and after the 80th fixed-capacity cycle, the peaks of Li_2O_2 were not found in the XRD pattern. The result demonstrates that the NCO-500 electrode exhibited an excellent cycling stability and can efficiently catalyse the formation and decomposition of Li_2O_2 during cycling. As shown in Fig. 5d, the urchin-like sphere was wrapped up with a Li_2O_2 film after the cell was fully discharged to 2.35 V. Whether Li_2O_2 was formed as particles or as films was controlled by the solubility of LiO_2.[84] The particle-shaped Li_2O_2 grew *via* a solution mechanism due to the high soluble LiO_2, while the film-shaped Li_2O_2 grew through a surface growth model of low soluble LiO_2. In this case, film-like Li_2O_2 was formed *via* a surface growth pathway on the urchin-like NiO–$NiCo_2O_4$ cathode, providing a large contact area between the discharge product and cathode surfaces.[85] As a benefit, the electron transfer during the charge process was facilitated, contributing to a reduced charge overpotential and good rechargeability.[86,87] After being recharged to 4.35 V, the

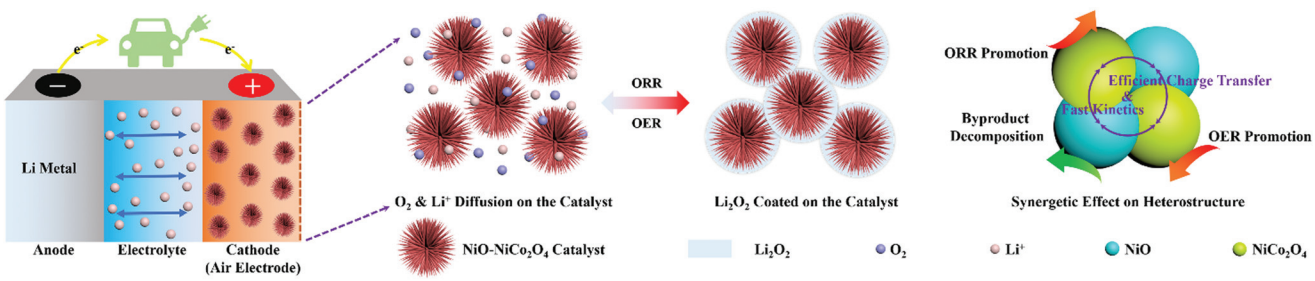

Fig. 6 Schematic illustration for the reaction mechanism during discharge and recharge process.

film disappeared, and the urchin-like structure of the NCO-500 electrode appeared again as shown in Fig. 5e. The morphology of the electrode also retained after 80th cycle at a fixed capacity of 600 mA h g^{-1}, as shown in Fig. 5f.

Fig. 6 shows the schematic illustration for the formation and decomposition of film-like Li_2O_2 during the discharge and recharge process in Li–O_2 batteries with the NiO–$NiCo_2O_4$ electrode. The urchin-like morphology promoted the diffusion of oxygen and electron and provided sufficient space for loading Li_2O_2 to mitigate volumetric variation during cycling. The heterostructure microspheres effectively prevented the diffusion of discharge products and accelerated electron transfer for Li_2O_2 conversion reactions. The synergetic effect among $NiCo_2O_4$, NiO and the heterostructure also contributed to the superior electrocatalytic ability of NiO–$NiCo_2O_4$ electrodes.[57] Therefore, this NiO–$NiCo_2O_4$ heterostructure exhibited excellent electrocatalytic performance in Li–O_2 batteries.

4. Conclusions

In summary, urchin-like NiO–$NiCo_2O_4$ microspheres with heterostructures were successfully synthesized through a facile hydrothermal-assisted method and presented favourable catalytic activity towards both the ORR and the OER for non-aqueous Li–O_2 batteries. The assembled batteries employing NCO-500 as a catalyst delivered a high discharge/charge capacity of 9231/8349 mA h g^{-1} at the current density of 100 mA g^{-1}. Besides, NCO-500 also exhibited good rate capability and cycling stability. Even when the current density increased to 500 mA g^{-1}, discharge/charge capacities of 3711/2254 mA h g^{-1} were still achieved. When discharge/charge capacities are limited to 600 mA h g^{-1}, Li–O_2 batteries containing the NCO-500 electrode could be continuously cycled for 80 cycles without obvious terminal voltage variation and exhibited no capacity loss at the current density of 100 mA g^{-1}. This superior electrocatalytic performance resulted from the unique heterostructure of NiO–$NiCo_2O_4$. It can facilitate continuous oxygen flow and charge transport during cycle as well as provide enough reaction sites for Li_2O_2 deposition and decomposition. Furthermore, according to the reported literature,[57] the introduction of the NiO phase is likely to promote the decomposition of certain by-products. This study suggests that the NiO–$NiCo_2O_4$ microspheres with heterostructures are promising cathode catalyst materials for Li–O_2 batteries.

Conflicts of interest

There are no conflicts to declare.

Acknowledgements

This work was supported by the National Nature Science Foundation of China (No. 51672162), the China Postdoctoral Science Foundation (2017M622198), the Natural Science Foundation of Shandong Province (ZR2017BEM018), the Open Project Program of Key Laboratory for Analytical Science of Food Safety and Biology, Ministry of Education (FS18010) and the Fundamental Research Funds of Shandong University (No. 2017JC035).

Notes and references

1 (*a*) X. M. Lou, C. F. Lin, Q. Luo, J. B. Zhao, B. Wang, J. B. Li, Q. Shao, X. K. Guo, N. Wang and Z. H. Guo, *ChemElectroChem*, 2017, **4**, 3171–3180; (*b*) M. Idrees, S. Batool, J. Kong, Q. Zhuang, H. Liu, Q. Shao, N. Lu, Y. Feng, E. K. Wujcik, Q. Gao, T. Ding, R. Wei and Z. Guo, *Electrochim. Acta*, 2019, **296**, 925–937; (*c*) Y. Guo, Y. Li, X. Lou, J. Guan, Y. Li, X. Mai, H. Liu, C. X. Zhao, N. Wang, C. Yan, G. Gao, H. Yuan, J. Dai, R. Su and Z. Guo, *J. Mater. Sci.*, 2018, **53**, 13790–13800; (*d*) J. Guan, H. Xiao, X. Lou, Y. Guo, X. Luo, Y. Li, C. Yan, X. Yan, G. Gao, H. Yuan, J. Dai, R. Su and Z. Guo, *ES Energy. Environ.*, 2018, **1**, 80–88.

2 C. F. Lin, L. Hu, C. B. Cheng, K. Sun, X. K. Guo, Q. Shao, J. Li, N. Wang and Z. H. Guo, *Electrochim. Acta*, 2018, **260**, 65–72.

3 R. J. Li, C. F. Lin, N. Wang, L. J. Luo, Y. J. Chen, J. B. Li and Z. H. Guo, *Adv. Compos. Hybrid Mater.*, 2018, **1**, 440–459.

4 J. Guan, H. Y. Xiao, X. Y. Lou, Y. G. Guo, X. M. Luo, Y. S. Li, C. Yan, X. R. Yan, G. L. Gao, H. Yuan, J. Da, R. J. Su, W. X. Gu and Z. H. Guo, *Eng. Sci.*, 2018, **1**, 80–88.

5 X. C. Zhao, P. Yang, L. J. Yang, Y. Cheng, H. Y. Chen, H. Liu, G. Wang, V. Murugadoss, S. Angaiah and Z. H. Guo, *ES Mater. Manuf.*, 2018, **1**, 67–71.

6 S. L. Zhai, L. Wei, H. E. Karahan, Y. Q. Wang, C. J. Wang, A. Montoya, Q. Shao, X. Wang and Y. Chen, *Carbon*, 2018, **132**, 698–708.

7 L. K. Yang, X. Wang, X. M. Mai, T. Wang, C. Wang, X. Li, V. Murugadoss, Q. Shao, S. Angaiah and Z. H. Guo, *J. Colloid Interface Sci.*, 2019, **534**, 459–468.

8 Y. Li, L. L. Zou, J. Li, K. Guo, X. W. Dong, X. W. Li, X. Z. Xue, H. F. Zhang and H. Yang, *Electrochim. Acta*, 2014, **129**, 14–20.

9 G. X. Liu, L. Zhang, S. Q. Wang, L. X. Ding and H. H. Wang, *J. Mater. Chem. A*, 2017, **5**, 14530–14536.

10 J. Christensen, P. Albertus, R. S. Sanchez Carrera, T. Lohmann, B. Kozinsky, R. Liedtke, J. Ahmed and A. Kojic, *J. Electrochem. Soc.*, 2012, **159**, R1–R30.

11 W. B. Luo, X. W. Gao, D. Q. Shi, S. L. Chou, J. Z. Wang and H. K. Liu, *Small*, 2016, **12**, 3031–3038.

12 K. M. Liao, X. B. Wang, Y. Sun, D. M. Tang, M. Han, P. He, X. F. Jiang, T. Zhang and H. S. Zhou, *Energy Environ. Sci.*, 2015, **8**, 1992–1997.

13 Y. Zhang, L. Qian, W. Zhao, X. M. Li, X. S. Huang, X. M. Mai, Z. K. Wang, Q. Shao, X. R. Yan and Z. H. Guo, *J. Electrochem. Soc.*, 2018, **165**, H510–H516.

14 Z. Y. Guo, D. D. Zhou, X. L. Dong, Z. J. Qiu, Y. G. Wang and Y. Y. Xia, *Adv. Mater.*, 2013, **25**, 5668–5672.

15 H. G. Jung, J. Hassoun, J. B. Park, Y. K. Sun and B. Scrosati, *Nat. Chem.*, 2012, **4**, 579–585.
16 Z. L. Jian, P. Liu, F. J. Li, P. He, X. W. Guo, M. W. Chen and H. S. Zhou, *Angew. Chem., Int. Ed.*, 2014, **53**, 442–446.
17 Z. Y. Guo, G. N. Zhu, Z. J. Qiu, Y. G. Wang and Y. Y. Xia, *Electrochem. Commun.*, 2012, **25**, 26–29.
18 J. J. Xu, Z. L. Wang, D. Xu, L. L. Zhang and X. B. Zhang, *Nat. Commun.*, 2013, **4**, 2438.
19 M. Leskes, N. E. Drewett, L. J. Hardwick, P. G. Bruce, G. R. Goward and C. P. Grey, *Angew. Chem., Int. Ed.*, 2012, **51**, 8560–8563.
20 B. Sun, J. Q. Zhang, P. Munroe, H. J. Ahn and G. X. Wang, *Electrochem. Commun.*, 2013, **31**, 88–91.
21 F. Li, D. M. Tang, Y. Chen, D. Golberg, H. Kitaura, T. Zhang, A. Yamada and H. Zhou, *Nano Lett.*, 2013, **13**, 4702–4707.
22 X. F. Hu, X. P. Han, Y. X. Hu, F. Y. Cheng and J. Chen, *Nanoscale*, 2014, **6**, 3522–3525.
23 D. Oh, J. Qi, Y. C. Lu, Y. Zhang, Y. Shao Horn and A. M. Belcher, *Nat. Commun.*, 2013, **4**, 2756.
24 F. J. Li, D. M. Tang, Z. L. Jian, D. Q. Liu, D. Golberg, A. Yamada and H. S. Zhou, *Adv. Mater.*, 2014, **26**, 4659–4664.
25 J. Lu, L. Cheng, K. C. Lau, E. Tyo, X. Y. Luo, J. G. Wen, D. Miller, R. S. Assary, H. H. Wang, P. Redfern, H. M. Wu, J. B. Park, Y. K. Sun, S. Vajda, K. Amine and L. A. Curtiss, *Nat. Commun.*, 2014, **5**, 4895.
26 W. H. Ryu, T. H. Yoon, S. H. Song, S. Jeon, Y. J. Park and I. D. Kim, *Nano Lett.*, 2013, **13**, 4190–4197.
27 L. L. Huang, Y. J. Mao, G. Q. Wang, X. K. Xia, J. Xie, S. C. Zhang, G. H. Du, G. S. Cao and X. B. Zhao, *NewJ. Chem.*, 2016, **40**, 6812–6818.
28 J. K. Wang, R. Gao, D. Zhou, Z. J. Chen, Z. H. Wu, G. Schumacher, Z. B. Hu and X. F. Liu, *ACS Catal.*, 2017, **7**, 6533–6541.
29 L. T. Yan, H. Z. Wang, D. Huang and H. M. Luo, *Eng. Sci.*, 2018, **1**, 4–20.
30 Y. Cao, Z. K. Wei, J. He, J. Zang, Q. Zhang, M. S. Zheng and Q. F. Dong, *Energy Environ. Sci.*, 2012, **5**, 9765–9768.
31 S. Y. Liu, Y. G. Zhu, J. Xie, Y. Huo, H. Y. Yang, T. J. Zhu, G. S. Cao, X. B. Zhao and S. C. Zhang, *Adv. Energy Mater.*, 2014, **4**, 1301960.
32 G. Q. Wang, L. L. Huang, W. Huang, J. Xie, G. H. Du, S. C. Zhang, P. Y. Zhu, G. S. Cao and X. B. Zhao, *Nanoscale*, 2015, **7**, 20614–20624.
33 S. C. Ma, L. Q. Sun, L. N. Cong, X. G. Gao, C. Yao, X. Guo, L. H. Tai, P. Mei, Y. P. Zeng, H. M. Xie and R. S. Wang, *J. Phys. Chem. C*, 2013, **117**, 25890–25897.
34 H. L. Wang, Y. Yang, Y. Y. Liang, G. Y. Zheng, Y. G. Li, Y. Cui and H. J. Dai, *Energy Environ. Sci.*, 2012, **5**, 7931–7935.
35 L. Zou, J. F. Cheng, Y. X. Jiang, Y. P. Gong, B. Chi, J. Pu and L. Jian, *RSC Adv.*, 2016, **6**, 31248–31255.
36 S. J. Peng, Y. X. Hu, L. L. Li, X. P. Han, F. Y. Cheng, M. Srinivasan, Q. Y. Yan, S. Ramakrishna and J. Chen, *Nano Energy*, 2015, **13**, 718–726.
37 C. Shen, Z. Y. Wen, F. Wang, K. Rui, Y. Lu and X. W. Wu, *J. Power Sources*, 2015, **294**, 593–601.
38 D. A. Agyeman, M. Park and Y. M. Kang, *J. Mater. Chem. A*, 2017, **5**, 22234–22241.
39 J. Wang, T. Qiu, X. Chen, Y. L. Lu and W. S. Yang, *J. Power Sources*, 2014, **268**, 341–348.
40 L. Y. Li, L. F. Shen, P. Nie, G. Pang, J. Wang, H. S. Li, S. Y. Dong and X. G. Zhang, *J. Mater. Chem. A*, 2015, **3**, 24309–24314.
41 B. Kirubasankar, V. Murugadoss, J. Lin, T. Ding, M. Y. Dong, H. Liu, J. X. Zhang, T. X. Li, N. Wang, Z. H. Guo and S. Angaiah, *Nanoscale*, 2018, **10**, 20414–20425.
42 B. Song, T. T. Wang, H. G. Sun, Q. Shao, J. K. Zhao, K. K. Song, L. H. Hao, L. Wang and Z. H. Guo, *Dalton Trans.*, 2017, **46**, 15769–15777.
43 T. M. Su, Q. Shao, Z. Z. Qin, Z. H. Guo and Z. L. Wu, *ACS Catal.*, 2018, **8**, 2253–2276.
44 Y. Ma, M. L. Ma, X. Q. Yin, Q. Shao, N. Lu, Y. N. Feng, Y. Lu, E. K. Wujcik, X. M. Mai, C. Wang and Z. H. Guo, *Polymer*, 2018, **156**, 128–135.
45 L. J. Wang, T. Zhu, Z. Y. Lyu, J. Zhang, L. L. Gong, S. N. Xiao, J. Liu, W. H. Dong, X. H. Cui, G. W. Ho and W. Chen, *RSC Adv.*, 2016, **6**, 98867–98873.
46 L. X. Zhang, S. L. Zhang, K. J. Zhang, G. J. Xu, X. He, S. M. Dong, Z. H. Liu, C. S. Huang, L. Gu and G. L. Cui, *Chem. Commun.*, 2013, **49**, 3540–3542.
47 B. Sun, X. D. Huang, S. Q. Chen, Y. F. Zhao, J. Q. Zhang, P. Munroe and G. X. Wang, *J. Mater. Chem. A*, 2014, **2**, 12053–12059.
48 W. M. Liu, T. T. Gao, Y. Yang, Q. Sun and Z. W. Fu, *Phys. Chem. Chem. Phys.*, 2013, **15**, 15806–15810.
49 X. Y. Yu, X. Z. Yao, T. Luo, Y. Jia, J. H. Liu and X. J. Huang, *ACS Appl. Mater. Interfaces*, 2014, **6**, 3689–3695.
50 K. R. Yoon, G. Y. Lee, J. W. Jung, N. H. Kim, S. O. Kim and I. D. Kim, *Nano Lett.*, 2016, **16**, 2076–2083.
51 W. Yin, Y. Shen, F. Zou, X. L. Hu, B. Chi and Y. H. Huang, *ACS Appl. Mater. Interfaces*, 2015, **7**, 4947–4954.
52 X. F. Hu, F. Y. Cheng, N. Zhang, X. P. Han and J. Chen, *Small*, 2015, **11**, 5545–5550.
53 P. Tan, W. Shyy, M. C. Wu, Y. Y. Huang and T. S. Zhao, *J. Power Sources*, 2016, **326**, 303–312.
54 (*a*) Y. Zheng, T. F. Zhou, C. F. Zhang, J. F. Mao, H. K. Liu and Z. P. Guo, *Angew. Chem., Int. Ed.*, 2016, **55**, 3408–3413; (*b*) Z. Zhao, R. Guan, J. Zhang, Z. Zhao and P. Bai, *Acta Metall. Sin. (Engl. Lett.)*, 2017, **30**, 66–72; (*c*) Z. Zhao, P. Bai1, R. Guan, V. Murugadoss, H. Liu, X. Wang and Z. Guo, *Mater. Sci. Eng., A*, 2018, **734**, 200–209; (*d*) Y. Zhao, L. Qi, Y. Jin, *et al.*, *J. Alloys Compd.*, 2015, **647**, 1104–1110; (*e*) Y. Zhao, S. Deng, H. Liu, J. Zhang, Z. Guo and H. Hou, *Comput. Mater. Sci.*, 2018, **154**, 365–370; (*f*) C. Wang, Z. He, X. Xie, X. Mai, Y. Li, T. Li, M. Zhao, C. Yan, H. Liu, E. Wujcik and Z. Guo, *Macromol. Mater. Eng.*, 2018, **3**, 1700462; (*g*) Z. Wang, H. Zhu, N. Cao, R. Du, Y. Liu and G. Zhao, *Mater. Lett.*, 2017, **186**, 274–278; (*h*) C. Wang, B. Mo, Z. He, Q. Shao, D. Pan, E. Wujick,

J. Guo, X. Xie, X. Xie and Z. Guo, *J. Membr. Sci.*, 2018, **556**, 118–125.

55 (*a*) W. W. Zhou, C. W. Cheng, J. P. Liu, Y. Y. Tay, J. Jiang, X. T. Jia, J. X. Zhang, H. Gong, H. H. Hng, T. Yu and H. J. Fan, *Adv. Funct. Mater.*, 2011, **21**, 2439–2445; (*b*) L. Zhang, M. Qin, W. Yu, Q. Zhang, H. Xie, Z. Sun, Q. Shao, X. Guo, L. Hao, Y. Zheng and Z. Guo, *J. Electrochem. Soc.*, 2017, **164**, H1086–H1090; (*c*) L. Zhang, W. Yu, C. Han, J. Guo, Q. Zhang, H. Xie, Q. Shao, Z. Sun and Z. Guo, *J. Electrochem. Soc.*, 2017, **164**, H651–H656; (*d*) C. Wang, B. Mo, Z. He, C. X. Zhao, L. Zhang, Q. Shao, X. Guo, E. Wujcik and Z. Guo, *Polymer*, 2018, **138**, 363–368.

56 (*a*) L. Y. Hu, C. L. Dai, H. Liu, Y. Li, B. L. Shen, Y. M. Chen, S. J. Bao and M. W. Xu, *Adv. Energy Mater.*, 2018, 1800709; (*b*) D. Jiang, V. Murugadoss, Y. Wang, J. Lin, T. Ding, Z. Wang, Q. Shao, C. Wang, H. Liu, N. Lu, R. Wei, S. Angaiah and Z. Guo, *Polym. Rev.*, 2018, DOI: 10.1080/15583724.2018.1546737, in press (*c*) W. Du, X. Wang, J. Zhan, X. Sun, L. Kang, F. Jiang, X. Zhang, Q. Shao, M. Dong, H. Liu, V. Murugadoss and Z. Guo, *Electrochim. Acta*, 2019, **296**, 907–915; (*d*) L. Wang, H. Qiu, C. Liang, P. Song, Y. Han, Y. Han, J. Gu, J. Kong, D. Pan and Z. Guo, *Carbon*, 2019, **141**, 506–514; (*e*) H. Liu, Q. Li, S. Zhang, R. Yin, X. Liu, Y. He, K. Dai, C. Shan, J. Guo, C. Liu, C. Shen, X. Wang, N. Wang, Z. Wang, R. Wei and Z. Guo, *J. Mater. Chem. C*, 2018, **6**, 12121–12141.

57 M. Hong, H. C. Choi and H. R. Byon, *Chem. Mater.*, 2015, **27**, 2234–2241.

58 S. F. Tong, M. B. Zheng, Y. Lu, Z. X. Lin, J. Li, X. P. Zhang, Y. Shi, P. He and H. S. Zhou, *J. Mater. Chem. A*, 2015, **3**, 16177–16182.

59 J. Y. Tian, Q. Shao, X. J. Dong, J. L. Zheng, D. Pan, X. Y. Zhang, H. L. Cao, L. H. Hao, J. R. Liu, X. M. Mai and Z. H. Guo, *Electrochim. Acta*, 2018, **261**, 236–245.

60 P. Tan, Z. H. Wei, W. Shyy, T. S. Zhao and X. B. Zhu, *Energy Environ. Sci.*, 2016, **9**, 1783–1793.

61 B. Liu, P. Yan, W. Xu, J. Zheng, Y. He, L. Luo, M. E. Bowden, C. M. Wang and J. G. Zhang, *Nano Lett.*, 2016, **16**, 4932–4939.

62 A. Shanmugavani and R. K. Selvan, *Electrochim. Acta*, 2016, **189**, 283–294.

63 C. Wei, Y. Huang, M. H. Chen, J. Yan, W. Yao and X. F. Chen, *J. Colloid Interface Sci.*, 2017, **504**, 1–11.

64 J. Zhao, Z. J. Li, M. Zhang, A. Meng and Q. D. Li, *ACS Sustainable Chem. Eng.*, 2016, **4**, 3598–3608.

65 X. J. Liu, J. F. Liu and X. M. Sun, *J. Mater. Chem. A*, 2015, **3**, 13900–13905.

66 F. T. Ran, X. B. Yang and L. Shao, *Adv. Compos. Hybrid Mater.*, 2018, **1**, 32–55.

67 D. P. Lapham and A. C. C. Tseung, *J. Mater. Sci.*, 2004, **39**, 251–264.

68 L. Wei, K. Lozano and Y. B. Mao, *Eng. Sci.*, 2018, **3**, 62–66.

69 Y. N. Feng, E. Witkoske, E. S. Bell, Y. Wang, A. Tzempelikos, I. T. Ferguson and N. Lu, *ES Mater. Manuf.*, 2018, **1**, 13–20.

70 Q. Q. Tang, M. M. Chen, L. Wang and G. C. Wang, *J. Power Sources*, 2015, **273**, 654–662.

71 C. Mahala and M. Basu, *ACS Omega*, 2017, **2**, 7559–7567.

72 J. F. Marco, J. R. Gancedo, M. Gracia, J. L. Gautier, E. I. Ríos, H. M. Palmer, C. Greaves and F. J. Berry, *J. Mater. Chem.*, 2001, **11**, 3087–3093.

73 D. L. Liu, C. Zhang, Y. F. Yu, Y. M. Shi, Y. Yu, Z. Q. Niu and B. Zhang, *Nano Res.*, 2017, **11**, 603–613.

74 C. Chang, L. Zhang, C. W. Hsu, X. F. Chuah and S. Y. Lu, *ACS Appl. Mater. Interfaces*, 2018, **10**, 417–426.

75 X. F. Lu, D. J. Wu, R. Z. Li, Q. Li, S. H. Ye, Y. X. Tong and G. R. Li, *J. Mater. Chem. A*, 2014, **2**, 4706–4713.

76 J. Zhang, F. Liu, J. P. Cheng and X. B. Zhang, *ACS Appl. Mater. Interfaces*, 2015, **7**, 17630–17640.

77 J. M. Xu, J. S. Wu, L. L. Luo, X. Q. Chen, H. B. Qin, V. Dravid, S. B. Mi and C. L. Jia, *J. Power Sources*, 2015, **274**, 816–822.

78 E. Jokar, A. I. Zad and S. Shahrokhian, *J. Solid State Electrochem.*, 2014, **19**, 269–274.

79 S. Lau and L. A. Archer, *Nano Lett.*, 2015, **15**, 5995–6002.

80 L. L. Liu, H. P. Guo, Y. Y. Hou, J. Wang, L. J. Fu, J. Chen, H. K. Liu, J. Z. Wang and Y. P. Wu, *J. Mater. Chem. A*, 2017, **5**, 14673–14681.

81 B. D. McCloskey, R. Scheffler, A. Speidel, D. S. Bethune, R. M. Shelby and A. C. Luntz, *J. Am. Chem. Soc.*, 2011, **133**, 18038–18041.

82 S. A. Freunberger, Y. H. Chen, N. E. Drewett, L. J. Hardwick, F. Barde and P. G. Bruce, *Angew. Chem., Int. Ed.*, 2011, **50**, 8609–8613.

83 L. L. Liu, J. Wang, Y. Hou, J. Chen, H. K. Liu, J. Z. Wang and Y. P. Wu, *Small*, 2016, **12**, 602–611.

84 Z. Sadighi, J. P. Liu, F. Ciucci and J. K. Kim, *Nanoscale*, 2018, **10**, 15588–15599.

85 F. L. Meng, Z. W. Chang, J. J. Xu, X. B. Zhang and J. M. Yan, *Mater. Horiz.*, 2018, **5**, 298–302.

86 X. Z. Ren, M. J. Huang, S. Luo, Y. L. Li, L. B. Deng, H. W. Mi, L. N. Sun and P. X. Zhang, *J. Mater. Chem. A*, 2018, **6**, 10856–10867.

87 Y. Xing, Y. Yang, R. J. Chen, M. C. Luo, N. Chen, Y. S. Ye, J. Qian, L. Li, F. Wu and S. J. Guo, *Small*, 2018, **14**, 1704366.